Volume 39
Number 4
April 2024
Pages 987–1178

JAAS

Journal of Analytical Atomic Spectrometry

rsc.li/jaas

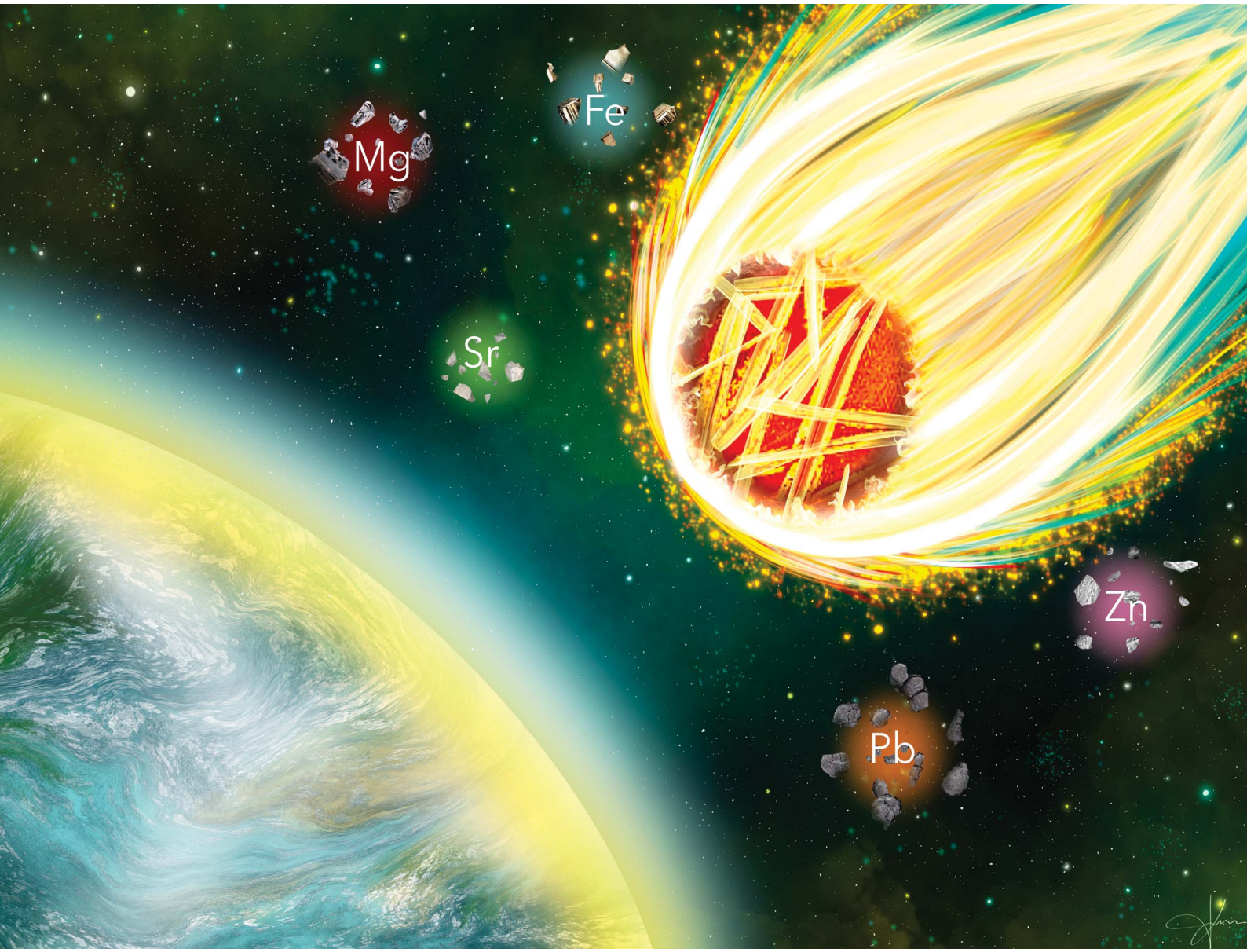

ISSN 0267-9477

ROYAL SOCIETY OF CHEMISTRY

PAPER

Frank Vanhaecke *et al.*

Analytical capabilities of LA-ICP-ToF-MS for ultra-fast 2D quantitative elemental mapping of micrometeorites

JAAS

ROYAL SOCIETY OF CHEMISTRY

PAPER

View Article Online
View Journal | View Issue

Cite this: J. Anal. At. Spectrom., 2024, 39, 1050

Analytical capabilities of LA-ICP-ToF-MS for ultra-fast 2D quantitative elemental mapping of micrometeorites†

Stepan M. Chernonozhkin, [ab] Thibaut Van Acker, [a] Stijn J. M. Van Malderen, [ac] Joke Belza,[a] Steven Goderis [d] and Frank Vanhaecke *[a]

Time-of-flight ICP-mass spectrometry (ICP-ToF-MS) allows acquisition of almost the entire periodic table in only a few tens of microseconds, with several mass spectra combined into a single readout. When hyphenated with a low-dispersion laser ablation (LA) unit, it allows for 2D elemental mapping at a laser repetition rate of several hundred hertz, with each laser shot recorded as a single pixel. Although its use in geosciences is increasing, the technique is often referred to as semi-quantitative. Here, we present the outcomes of ultra-fast high-resolution 2D mapping and quantification of the constituting elements of geological reference materials and micrometeorites with LA-ICP-ToF-MS, carried out in a period of over a year. Quantitative data for each pixel were obtained through a combination of multi-point external calibration and normalization of the sum of all element oxide contents to 100%. Detection limits ranging from 0.1 to 10 μg g^{-1} were attained for most elements when using a 5 μm × 5 μm square laser spot. Repeated analysis of reference materials in a period of over one year demonstrates an intermediate precision down to 3% RSD.

Received 2nd October 2023
Accepted 12th January 2024

DOI: 10.1039/d3ja00335c

rsc.li/jaas

Introduction

Since its first reported use in 1993,[1] time-of-flight ICP-mass spectrometry (ICP-ToF-MS) has found its niche in monitoring fast transient signals[2] due to its ability to detect ions from all elements of the periodic table (Na to U) at a time scale of just few milliseconds (the ICP-ToF-MS instrument used in this work has a base integration time of 46 μs, but at least 60 spectra are aggregated in a single readout, practically equivalent to a 300 Hz acquisition rate).[3] Common scanning-based ICP-MS units would require a couple of hundred milliseconds to scan a similar set of elements. Moreover, with scanning-based ICP-MS, the nuclides of interest need to be identified prior to the 2D mapping. Recently, low-dispersion ablation cells and aerosol transport systems were developed for laser ablation (LA) systems and have become commercially available. These ablation cells display improved aerosol transport and greatly shortened the duration of single pulse responses to approximately 1 ms (full width at 1% maximum).[4–9] Hyphenated with ICP-ToF-MS, low-dispersion LA allows for ultra-fast 2D mapping (0.3–30 mm^2 h^{-1}) at μm scale lateral resolution and 100–1000 Hz laser pulse repetition frequency, while almost the entire periodic table is recorded for each laser shot, and thus, each pixel of the elemental map generated. As such 2D map generation speed constitutes a significant improvement compared to what is possible using scanning-based LA-ICP-MS, it is often referred to as ultra-fast mapping. Despite the capability of the technique to provide quantitative data based on normalization of the sum of all element oxide levels to 100%,[10] rendering the approach independent from the necessity of a homogeneously distributed internal standard, the application of LA-ICP-ToF-MS 2D mapping to geomaterials remains relatively scarce.[11–13] Moreover, such element distribution maps are often referred to as semi-quantitative (a terminology not defined by IUPAC). The complexity of 100% oxide normalization strategies becomes evident when considering changing in the stoichiometry for different mineral phases and changes in fractionation behaviour due to varying thermal interaction with the surface.

Cosmic spherules (CSs), melted extra-terrestrial particles of 50–2000 μm in diameter, which survived atmospheric entry, are ideal targets for LA-ICP-ToF-MS mapping due to their relatively simple mineralogy dominated by olivine, pyroxene, and magnetite in glassy mesostasis. Predominantly glassy matrices limit potential non-stoichiometric effects related to differences in the interaction of the laser irradiation with mineral lattices.[14]

[a]Ghent University, Department of Chemistry, Atomic & Mass Spectrometry A&MS research unit, Campus Sterre, Krijgslaan 281 – S12, 9000, Ghent, Belgium. E-mail: frank.vanhaecke@ugent.be

[b]Montanuniversität Leoben, Chair of General and Analytical Chemistry, Franz Josef Straße 18, 8700, Leoben, Austria

[c]Teledyne Photon Machines, 384 Gallatin Park Dr, Bozeman, Montana 59715, USA

[d]Vrije Universiteit Brussel, Archaeology, Environmental Changes and Geo-Chemistry, Pleinlaan 2, 1050, Brussels, Belgium

† Electronic supplementary information (ESI) available. See DOI: https://doi.org/10.1039/d3ja00335c

Quantitative elemental data for CSs can aid in confirming the extraterrestrial nature of the particles, determining their primary parent body characteristics, constraining the modifications experienced during atmospheric entry, and refining the alteration histories of individual particles during their residence at the Earth's surface.[15] At the same time, the microscopic size of CSs necessitates the use of element distribution mapping techniques with high spatial resolution and multi-element capabilities, preferably being minimally destructive. Only electron microprobe analysis, synchrotron micro X-ray fluorescence spectrometry, and secondary ion mass spectrometry can provide similar 2D element distribution maps, but they have limitations in terms of detection limits, availability, sample throughput, quantification, and/or cost efficiency.

The major goal of this manuscript is to characterize the analytical capabilities of LA-ICP-ToF-MS with a low-dispersion ablation cell to generate quantitative 2D element distribution maps of geomaterials and to validate the quantitative nature of the measurement procedure, relying on external calibration against matrix-matched glass geological reference materials (GRMs), followed by normalization of the sum of all element oxide contents to 100%.

Experimental

Geological reference materials

GRMs with matrices corresponding to a range of natural rock compositions from the United States Geological Survey, USGS, Denver, USA (GSE-1G, GSD-1G – synthetic basaltic glass, BIR-1G, BHVO-2G, BCR-2G – basaltic glass, NKT-1G – nephelinitic glass)[16] and MPI-DING, Mainz, Germany (GOR128-G, GOR132-G – komatiitic glasses, ML3B-G, KL2-G – basaltic glasses, ATHO-G – rhyolitic glass, StHs6/80-G – andesitic glass, T1-G – dioritic glass)[17] have been used for multi-point external calibration and method validation. As a compilation of the calibrations from several different projects is presented here, different sessions contained a larger or smaller set of GRMs analysed. Certified data are preferentially used, but GeoReM values have been relied upon when the former are missing.

Micrometeorite sample collection

Five melted micrometeorites larger than 200 μm (barred olivine and cryptocrystalline types of CSs, and a scoriaceous/partially melted particle) were acquired during missions in the Antarctic and are described in detail elsewhere.[15,18] Briefly, the micrometeorites have been collected from sedimentary traps near the Widerøefjellet summit (altitude 2750 m), Sør Rondane Mountains, East Antarctica. The CSs have been cast into epoxy mounts and progressively polished with 1200–4000 grit size silicon carbide sandpaper and 4000 grit diamond paste, and preliminary characterized as described earlier.[18]

LA-ICP-ToF-MS setup

The LA-ICP-ToF-MS setup consisted of an Iridia (Teledyne Photon Machines, Bozeman, MT, USA) 193 nm ArF* excimer-based LA system, equipped with a Cobalt™ ablation chamber and a low-dispersion tube-type ablation cell, coupled to the torch of an icpTOF 2R (TOFWERK, Thun, Switzerland) ICP-mass spectrometer *via* the aerosol rapid introduction system (ARIS). The ICP-ToF-MS unit quasi-simultaneously detected signals over almost the entire elemental mass spectrum, m/z range 23–238 amu ($^{23}Na^+$ to $^{238}U^+$), in a time period of 46 μs. The determination of the lighter elements is complicated by their very short time of flight. Re-tuning for improved sensitivity in the lighter mass range is possible at the price of deteriorated sensitivities in the higher mass range.[19] Depending on the pixel acquisition rate for LA mapping (100–300 pixels per s), each 68–206 subsequent ICP-ToF-MS spectra were integrated into a single readout on-line for each laser shot/pixel. Each laser pulse triggered the mass spectrometer individually. The mass regions corresponding to $^{36}Ar^+$, $^{40}Ar^+$, $^{40}ArH^+$, and $^{40}Ar^{40}Ar^+$ were attenuated using a notch-filter quadrupole to avoid detector saturation. LA mapping of CSs and GRMs was carried out at 0.3–30 $mm^2\ h^{-1}$, with laser spot sizes of 2 μm ϕ, 3 μm ϕ, or 5 μm × 5 μm square at a fluence of 2 J cm^{-2} and a laser repetition rate of 100–300 Hz. A detailed description of the setup can be found in an earlier publication.[11]

Analytical workflow

A typical analytical session consisted of the measurement of: (i) gas blanks, (ii) all glass GRMs relied on for external calibration, (iii) 1 to 3 CSs, followed by (iv) blanks, and (v) all glass GRMs again. Each analysis of a GRM and a gas blank (measured with the laser shutter closed) consisted of mapping of a small area of the GRM with 10 adjacent laser lines, each ≈1 mm long using the same laser parameters as used for the samples. The analysis of each GRM was repeated 3–5 times before and 3–5 times after the analysis of the samples. The mass spectra were recorded and preliminarily processed in the Tofpilot v2.8 software. Preliminary processing included mass calibration, baseline modelling and subtraction, peak integration, and integration of the mass spectra belonging to each individual laser shot/pixel. HDIP software (Teledyne Photon Machines, Bozeman, MT, USA) was used for data post-processing, including calculation of limits of detection (LoDs), external calibration, sum normalization of the oxide levels to 100%, automatic selection of volumes of interest (VOIs) within the 2D elemental maps of the micrometeorite samples (each VOI belongs to a section or a mineral phase with a composition distinctively different from the other, and can be selected using various mathematical algorithms or manually), integration of VOIs, and exporting the quantitative elemental maps. BHVO-2G and StHs6/80-G GRMs were selected to be processed as secondary QC materials together with samples in every analytical session (these GRMs were measured in 8 and 6 sessions, respectively, as each session belonged to different projects with different time constraints and requirements for calibration).

Results and discussion

The calibration curves obtained for a few elements based on least squares regression of the data obtained during a single

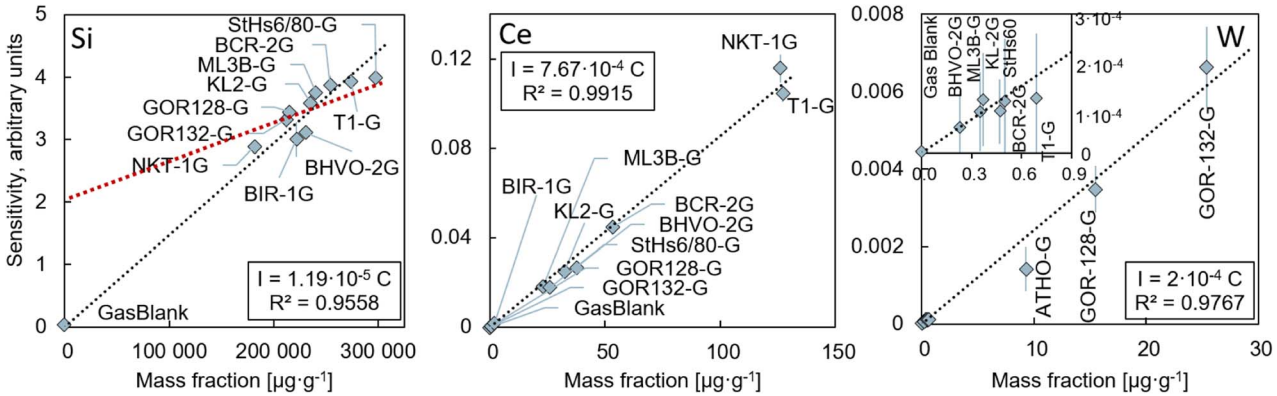

Fig. 1 Calibration lines for LA-ICP-ToF-MS mapping for Si, Ce, and W (left to right). Each point is based on an average of 10 integrated 2D LA-ICP-ToF-MS maps for a GRM (or a gas blank) at the beginning and at the end of the session; error bars correspond to 2SD. Red dashed line – calibration line for Si without forcing it through the origin and not including the gas blank.

analytical session are shown in Fig. 1. The plots demonstrate a good linear fit, even when the element concentrations are spread over a range of 2 orders of magnitude (*e.g.*, for W, Fig. 1). Based on experience, forcing the regression line through zero and involving the gas blank into the calibration line provides better results for micrometeorite samples, which can fall outside the calibration range. Fig. 1 shows an example of Si calibration lines when the regression is forced through zero and the gas blank is included (black dash line) relative to a similar regression involving GRMs only (red dashed line). Finally, not forcing the calibration line through the origin often results in an artificial bias for trace elements (typically for REE), for which the concentrations are close to the blank values, as the regression intercept is not correctly estimated in the regression model, either due to uncertainty in the measurement, or uncertainty in the reference value. Synthetic glasses (GSE-1G, GSD-1G) were not used for calibration of trace elements, as they tend to have unnaturally high mass fractions of many trace elements, which practically turns the regression lines into a single-point calibration approach. Normalization of the sum of the element oxide mass fractions to 100% after the multi-point external calibration is crucial in the absence of a suitable internal standard, as it corrects for variations in the ablation yield. The ratio of +II and +III Fe in the samples can be measured using one of the X-ray absorption techniques, but using a reasonable estimate of the Fe oxide stoichiometry results in accurate results. Determination of the mass fractions of major elements, especially Si, becomes critical, as this normalization will propagate any bias into the trace element data. We observed that for GRMs the best matching of the measured data with the certified values is achieved when multiple glass GRMs are used for Si calibration with an as large as possible spread in their Si mass fractions, involving high-Si felsic and low-Si mafic reference glasses (see Si in Fig. 1).

Limits of detection (LoDs) for 56 elements, as obtained in 7 mapping sessions over a period of 1 year, are shown in Fig. 2. The LoDs are calculated using the equation of Pettke *et al.*[20] using the gas blank data:

$$\mathrm{LoD} = \frac{\left(3.29 \times \sqrt{\left(R_{\mathrm{bkg}} \times \mathrm{DT} \times N_{\mathrm{an}} \times \left(1 + N_{\mathrm{an}}/N_{\mathrm{bkg}}\right)\right)} + 2.71\right)}{\left(N_{\mathrm{an}} \times \mathrm{DT} \times S\right)}$$

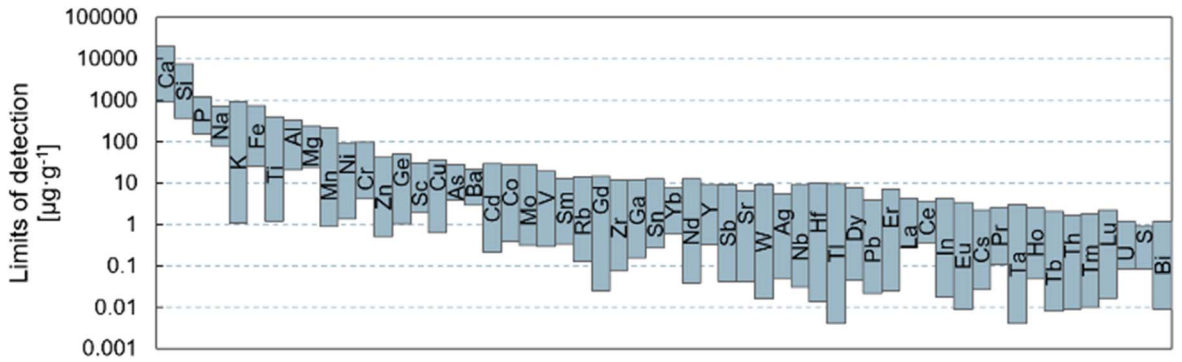

Fig. 2 Min–max range of limits of detection as obtained using LA-ICP-ToF-MS mapping of 0.004–0.05 mm^2 areas over a period of ~1 year. 2 µm ϕ circular, 3 µm ϕ circular, and 5 µm × 5 µm square laser spot sizes were used. Note that actual LoDs depend on multiple parameters other than the spot size. LoDs were calculated following Pettke *et al.*[20] Tuning of the mass analyzer may result in an improved sensitivity for the lower mass range, at the cost of sensitivity in the higher mass range.

in which R_{bkg} stands for the mean background count rate, DT is the dwell time, N_{bkg} and N_{an} are the number of sweeps for the background and analyte integration respectively, and S denotes the sensitivity. These LoDs correspond to 0.004–0.05 mm^2 integrated areas of the maps, and not to a single pixel. Despite a 5 μm × 5 μm square, 3 μm ϕ and 2 μm ϕ round laser spot was used only, LoDs down to 10 ng g^{-1} are attained for several trace elements, including some of the REE, and for most elements, the LoDs lie in the range of 0.1–10 μg g^{-1}. Such low LoDs are partially due to the very short signal pulse response offered by the combination of the low-dispersion tube-type ablation cell and aerosol rapid introduction system. This setup results in short temporally resolved pulses at the <1% baseline level, synchronized to the mass spectrometer cycle with individual pulse triggering. The delay between the trigger and the arrival of the aerosol is tuned daily before each session. In addition to the common factors affecting LoDs (memory effects, spectral interferences, isotopic abundances, and natural abundances of the elements in nature, *etc.*), in ICP-ToF-MS, notching of the m/z range around $^{40}Ar^+$, $^{38}Ar^+$ and $^{40}Ar^1H^+$ affects the LoDs of the neighboring elements (*e.g.* K, Fig. 2). In ICP-ToF-MS, notching of mass-to-charge ratios of Ar-related ions prior to the mass analyzer is required to prevent detector saturation.[21] The number of masses to be notched can be reduced if a collision reaction cell is operated with a reaction gas (*e.g.* H_2) that removes or strongly mitigates argide-based polyatomic ions by ion–molecule interactions.[22] Use of a collision reaction gas is also recommended as it can increase element sensitivities due to a collisional focusing effect.[21]

The long-term intermediate precision achievable using LA-ICP-ToF-MS was estimated *via* repeated 2D mapping of GRMs in 8 analytical sessions over a period of 1 year. The standard deviations thus obtained for 55 elements from integrated BHVO-2G maps ($n = 8$) are plotted as a function of their mass fraction in Fig. 3. For most elements with mass fractions of ≥10 μg g^{-1}, the intermediate precision is in a range of 5–15% (RSD), while it is still in a 5–30% (RSD) range for elements with a mass fraction <10 μg g^{-1}. At the same time, for some elements the data cannot be reliably quantified due to low intensities (*e.g.*, Cd, Cs, In), poor calibration (*e.g.* Ge, Ag, Sn, As) as a result of the absence of robust data for the GRMs and/or a potentially non-homogenous element distribution (*e.g.*, W), known in some GRMs, or due to spectral interference (*e.g.*, Ge). The poor calibration underlines the necessity of further interlaboratory characterization of the mass fractions of the elements concerned in common glass GRMs, preferably using high-precision isotope dilution for calibration.

The potential of a systematic bias was verified using glass GRMs displaying a natural rock composition. Results for a few elements based on integrated 2D maps collected during multiple sessions in a period of over a year are shown in Fig. 4. Even elements that suffer from poor calibration due to high uncertainty for the consensus values and that are present in the GRMs at sub-μg g^{-1} levels only can be quantified without systematic bias. For example, the measured mass fraction of W (see Fig. 1 and 4) in the integrated 2D maps of StHs6/80-G and BHVO-2 resulted in 0.35 ± 0.25 μg g^{-1} and 0.26 ± 0.18 μg g^{-1}, respectively, in a period of one year. Although these mass fractions are close to the LoD for W and have high

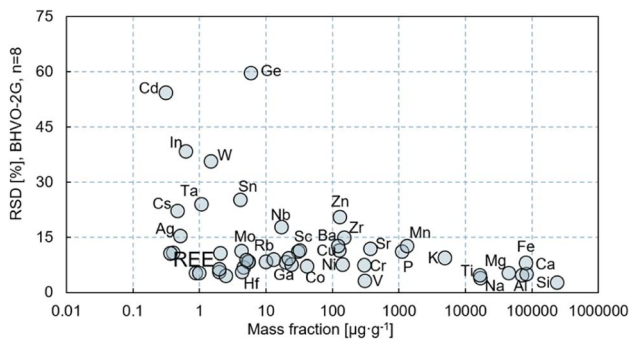

Fig. 3 Intermediate precision as obtained using LA-ICP-ToF-MS mapping, presented as a relative standard deviation for USGS BHVO-2G measured in 8 analytical sessions over a period of 1 year.

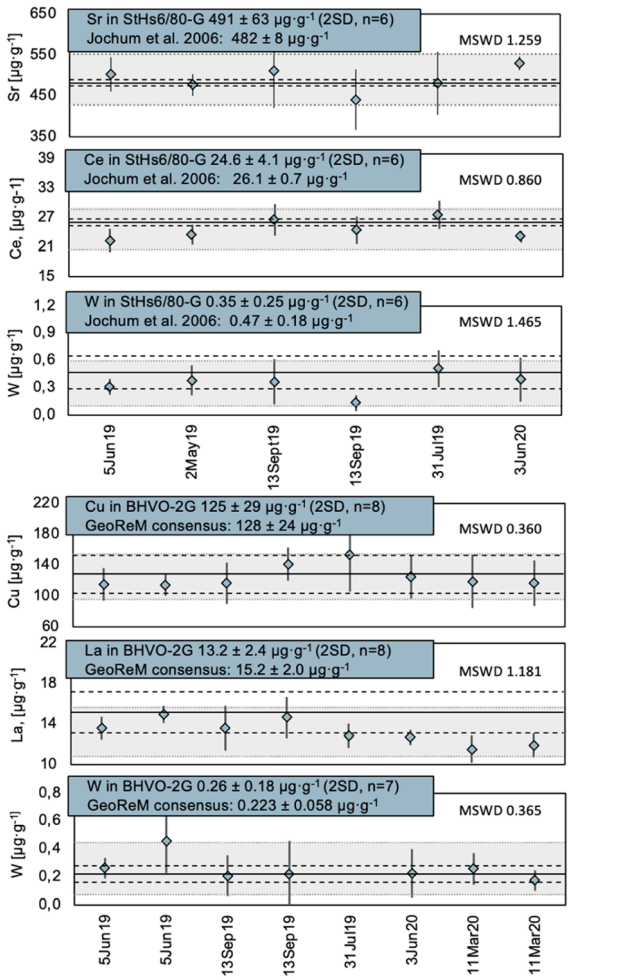

Fig. 4 Map-integrated values for Sr, Ce and W mass fractions in MPI-DING StHs6/80-G, and for Cu, La and W in USGS BHVO-2G. Grey bars represent the ±2SD range for the measured data. Dashed lines and solid lines represent the min–max range and the average for the consensus value (Jochum *et al.*[17] for StHs6/80-G and GeoRem consensus values for BHVO-2G).

measurement uncertainties as a result, the values fall within a range of the corresponding consensus values of 0.47 ± 0.18 μg g^{-1} and 0.223 ± 0.058 μg g^{-1}, indicating absence of systematic bias. Note that the mean squared weighted deviations (MSWD) for the Cu and W results in BHVO-2G is significantly lower than 1 (0.360 and 0.365, respectively), suggesting that the uncertainties of the individual measurements are overestimated (Fig. 4). This may result from inhomogeneity of the Cu and W distribution at the 3 μm scale, while it has no effect on the average value over the map.

Analysis of micrometeorites

Fig. 5 presents the LA-ICP-ToF-MS element mass fraction distribution maps of 4 melted (CS) micrometeorites and 1 scoriaceous (partially melted, Fig. 5C) one. Three of the 4 CSs are of the barred olivine type (Fig. 5A, D and E), while one has a cryptocrystalline texture (Fig. 5B). One of the barred olivine CSs contains a metal nugget and was heavily etched during terrestrial weathering (Fig. 5E).

After calibration, areas of the map with distinctly different compositions, corresponding to an individual phase (mineral or glassy metastasis, *e.g.* FeNi metal bead, olivine, magnetite grains – seen as bright spots in the SEM-BSE images, or melted and quenched glass) or filled-in vesicle can be identified and selected as VOI, either manually or automatically using a k-means clustering algorithm in the HDIP software. The scoriaceous micrometeorite (Fig. 5C) is highly vesicular, with a central filled cavity and relatively pristine partially melted vesicular outer rim, the mass fractions of which can be integrated individually. The outer rim of this micrometeorite is ≈100 μm thick and composed of glassy vesicular melt. Its central cavity is filled with ≈10 μm-sized mineral grains of background material. These mineral grains are too small to be robustly integrated as individual areas at 3 μm pixel size without including a significant number of pixels belonging to neighbouring phases or mixed-phase pixels. The barred olivine CSs (Fig. 5A, D and E) have thin outer margins of a few μm only, likely as a result of melting during the atmospheric passage and subsequent weathering in the Antarctic environment with local dissolution of the interstitial mesostasis. The effects of chemical weathering include the removal of primary mineral phases, such as olivine and glass, and incrustations by weathering products.[23] Such margins can be selected as individual VOIs by means of k-means clustering and integrated separately. The areas corresponding to the skeletal olivine and the glassy mesostasis of the barred olivine CS (Fig. 5A) were not integrated individually because they were found to have indistinguishable trace element compositions.

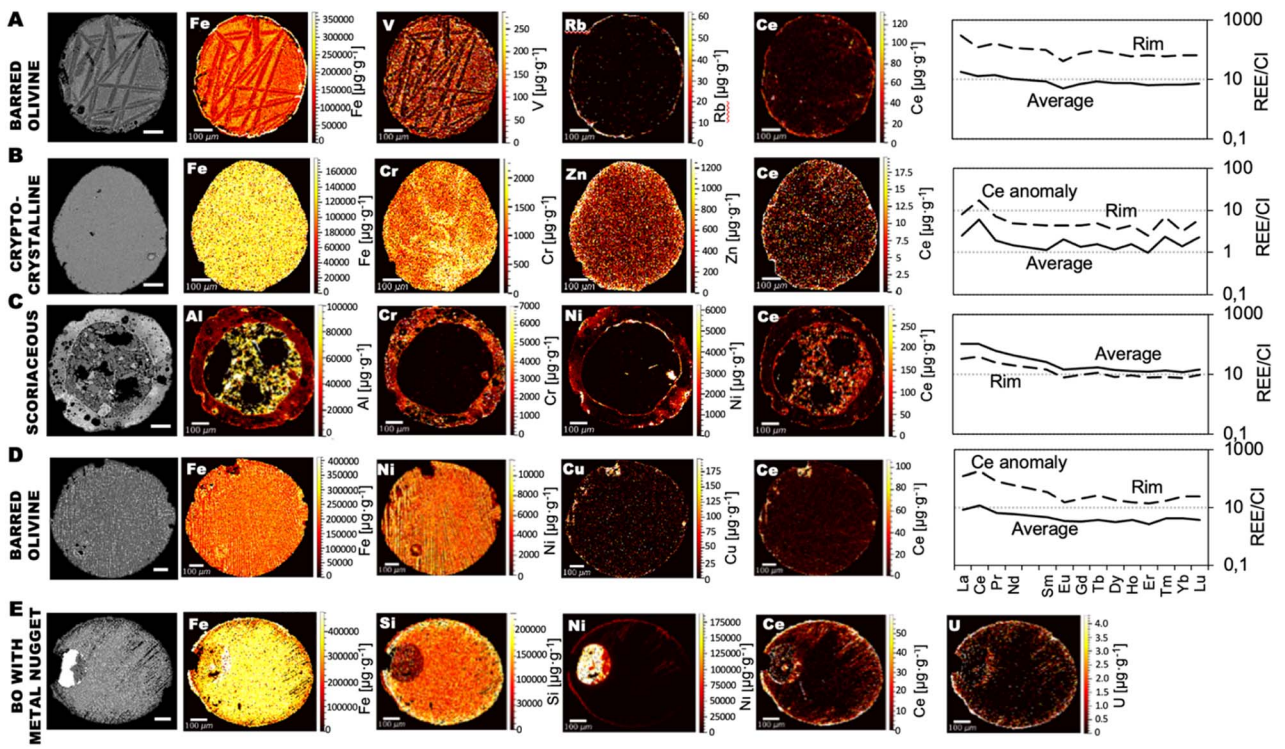

Fig. 5 Quantitative LA-ICP-ToF-MS 2D-maps for selected elements within 5 Antarctic micrometeorites and the REE patterns of the integrated areas normalized to average Solar System abundances (CI chondrite[24]) as measured with LA-ICP-ToF-MS. (A and D) Barred olivine CSs, (B) cryptocrystalline CS, (C) scoriaceous micrometeorite, (E) barred olivine CS with a metal nugget. On the left side, scanning electron microscope – backscattered electrons (SEM-BSE) images of the same micrometeorites are shown in grey scale. Note that the micrometeorite sections were gently polished after SEM-BSE analysis before the LA-ICP-ToF-MS mapping to remove the carbon conductive coating. The initial SEM images were rotated in an image processing software to align the orientation with the LA-ICP-ToF-MS maps. The space between Nd and Sm in the REE plots is for Pm, absent in nature.

The area corresponding to the Fe–Ni metal bead within the barred olivine CS in Fig. 5E could not be quantitatively characterized as the nanosecond pulse length of the LA system used in this work does not allow to ablate metal phases efficiently, and would require to be calibrated separately using reference materials with metallic matrices. In addition to the presence of a comparably altered particle rim (*e.g.*, Zn- and Ce-enriched zone), the cryptocrystalline CS (Fig. 5B) displays a complex pattern for Cr, which may reflect the distribution of primary phases (*e.g.*, olivine and chromite), which did not fully equilibrate during atmospheric melting. Calibration of pixels covering multiple mineral phases or edges between the mineral phase and embedding epoxy medium is challenging due to the unknown ratio of each phase, and thus, unknown normalization target values.

The REE patterns of both bulk micrometeorites and their selected melt areas (VOIs) are shown in Fig. 5 to demonstrate the quantitative capabilities of the LA-ICP-ToF-MS mapping approach. All micrometeorites have chondritic REE patterns, and overall elevated REE mass fractions compared to CI chondrites, following passive enrichment by evaporation during atmospheric entry. The bulk REE pattern of one barred olivine CS and one cryptocrystalline CS display a positive Ce anomaly (Fig. 5D). Cerium anomalies have previously been observed in CSs, as at highly oxidative conditions Ce can have oxidation states of +IV and +III, compared to the single +III oxidation state of the other REEs. As a result, Ce has a different behaviour during evaporation and terrestrial residence.[18] The narrow outer rims of all characterized CSs demonstrate elevated amounts of the REEs (Fig. 5A, B and D). The REE patterns of the scoriaceous micrometeorite and its outer melted layer are nearly identical, with the outer glassy layer overall being slightly depleted in REE compared to the filled central vesicle (Fig. 5C). Note an elevated mass fraction of Ni at the inner walls of the filled internal cavity of the scoriaceous micrometeorite (Fig. 5C), resulting from Ni back-condensation from the vapour phase.

Conclusions

Currently, low-dispersion LA-ICP-ToF-MS is largely seen as the method of choice for ultra-fast high-resolution 2D elemental mapping due to the possibility of using a very small laser spot size and high laser repetition rate. The mass range from Na to U is covered during each laser shot at 100–300 Hz [6] repetition rate, and each laser shot corresponds to a single pixel of the 2D map. Moreover, it is demonstrated here that the method is also capable of providing high-quality quantitative multi-element data of geological materials once the element contents are determined for each pixel following multi-point external calibration against natural glass GRMs and normalization of the sum of the oxide levels to 100%, and all pixels belonging to a specific area (VOI) are integrated. Mass fractions quantified in this way are demonstrated to show no systematic bias and display a much better precision than was initially expected for such ultra-fast multi-element mapping technique. Over a period of 1 year, the intermediate precision amounted to 5–15% (RSD) for most elements at a mass fraction $\geq$10 μg g^{-1}, and to 5–30% (RSD) for those at a mass fraction <10 μg g^{-1}. For some elements (*e.g.* Cd, Ge, In, Sn, As), however, no reliable quantitative data were obtained due to low signal intensities and/or absence of well-characterised GRMs for calibration. The LoDs obtained for elements in areas of geological materials mapped using LA-ICP-ToF-MS with 2 to 5 μm laser spot sizes are also significantly better than can be expected based on the general experience with LA-ICP-MS spot analysis. For most elements LoDs down to 0.1–10 μg g^{-1} were found when using a 5 μm × 5 μm laser beam, with values down to 10 ng g^{-1} for a few trace elements.

When applied to micrometeorites, LA-ICP-ToF-MS maps complement and extend petrographic observations. Chemically distinct regions of interest can be recognized within the maps, segmented either manually or automatically using statistical methods in the image processing software off-line, and quantified and normalized individually. Once calibrated, mass fractions of the micrometeorite components can be compared to the elemental patterns (*e.g.*, chondrite-normalized REE) of the bulk particle with the uncertainty levels demonstrated in this work. Compared to the traditional LA-ICP-MS spot analysis of geomaterials, the LA-ICP-ToF-MS mapping approach followed by selection and integration of VOIs (i) allows mass fractions of trace elements in microscopic zones or mineral phases of complex shape to be determined, (ii) does not require identification of the areas of interest prior to analysis, (iii) does not necessitate the determination of an internal standard with an independent method, and (iv) does not necessitate nuclides of interest to be identified before the analysis as a result of the full mass spectrum monitoring. (v) Moreover, LA-ICP-ToF-MS allows to work with fast single pulse responses, which also provide higher sensitivity due to aerosol compression, as well as higher throughput. (vi) In contrast to the traditional LA-ICP-MS analysis with typical 10–50 μm spot size, LA-ICP-ToF-MS is significantly less destructive, which is practical for valuable or rare geological sample sections (*e.g.*, future asteroid, Moon or Mars return missions).

Data availability

Quantitative information on the elemental composition of the reference materials measured in the course of this study are provided in tabular form in the ESI.† The source data for this paper can be provided by the first author upon request.

Author contributions

S. M. C.: conceptualization, investigation, formal analysis, visualization, writing of the original draft. T. V. A.: investigation, methodology, formal analysis, writing – review and editing. S. J. V. M.: software/hardware development, writing – review and editing. J. B.: investigation, writing – review and editing. S. G.: project administration, supervision, funding acquisition, resources (micrometeorite collection), writing – review and editing. F. V.: project administration, supervision, funding acquisition, writing – review and editing.

Conflicts of interest

S. J. V. M. and F. V. are inventors of patent WO2016042165A1, on which part of the technology of the Cobalt ablation cell used in this work is based. T. V. A. and F. V. conduct research at a research unit that has licensed intellectual property to Teledyne Photon Machines. S. J. V. M. is currently working as an employee of Teledyne Photon Machines.

Acknowledgements

S. M. C. and F. V. acknowledge the Flemish Research Foundation (FWO) for financial support ("Excellence of Science" project ET-HoME-ID30442502). S. M. C. acknowledges the funding from the Montanuniversität Leoben. T. V. A. acknowledges the FWO for his postdoctoral research fellowship (FWO.3E0.2022.0048.01). Collection of the micrometeorites investigated was made possible by the Belgian Science Policy through financial support for various projects (BELAM, Amundsen and BAMM).

References

1 D. P. Myers and G. M. Hieftje, *Microchem. J.*, 1993, **48**, 259–277.
2 O. Borovinskaya, B. Hattendorf, M. Tanner, S. Gschwind and D. Günther, *J. Anal. At. Spectrom.*, 2013, **28**, 226–233.
3 L. Hendriks, A. Gundlach-Graham, B. Hattendorf and D. Günther, *J. Anal. At. Spectrom.*, 2017, **32**, 548–561.
4 S. J. M. Van Malderen, J. T. van Elteren and F. Vanhaecke, *J. Anal. At. Spectrom.*, 2014, **30**, 119–125.
5 S. J. M. Van Malderen, T. Van Acker and F. Vanhaecke, *Anal. Chem.*, 2020, **92**, 5756–5764.
6 T. Van Acker, S. J. M. Van Malderen, T. Van Helden, C. Stremtan, M. Šala, J. T. van Elteren and F. Vanhaecke, *J. Anal. At. Spectrom.*, 2021, **36**, 1201–1209.
7 S. J. M. Van Malderen, A. J. Managh, B. L. Sharp and F. Vanhaecke, *J. Anal. At. Spectrom.*, 2016, **31**, 423–439.
8 H. A. O. Wang, D. Grolimund, C. Giesen, C. N. Borca, J. R. H. Shaw-Stewart, B. Bodenmiller and D. Günther, *Anal. Chem.*, 2013, **85**, 10107–10116.
9 C. Neff, P. Becker and D. Günther, *J. Anal. At. Spectrom.*, 2022, **37**, 677–683.
10 J. T. van Elteren, N. H. Tennent and V. S. Šelih, *Anal. Chim. Acta*, 2009, **644**, 1–9.
11 R. Maeda, T. Van Acker, F. Vanhaecke, A. Yamaguchi, V. Debaille, P. Claeys and S. Goderis, *J. Anal. At. Spectrom.*, 2023, **38**, 369–381.
12 D. Chew, K. Drost, J. H. Marsh and J. A. Petrus, *Chem. Geol.*, 2021, **559**, 119917.
13 M. Burger, A. Gundlach-Graham, S. Allner, G. Schwarz, H. A. O. Wang, L. Gyr, S. Burgener, B. Hattendorf, D. Grolimund and D. Günther, *Anal. Chem.*, 2015, **87**, 8259–8267.
14 D. Günther and B. Hattendorf, in *Laser Ablation ICP-MS in the Earth Sciences: Principles and Applications*, Mineralogical Association of Canada, 2007, vol. 29.
15 F. Van Maldeghem, M. van Ginneken, B. Soens, F. Kaufmann, S. Lampe, L. Krämer Ruggiu, L. Hecht, P. Claeys and S. Goderis, *Geochim. Cosmochim. Acta*, 2023, **354**, 88–108.
16 K. P. Jochum, M. Willbold, I. Raczek, B. Stoll and K. Herwig, *Geostand. Geoanal. Res.*, 2005, **29**, 285–302.
17 K. P. Jochum, B. Stoll, K. Herwig, M. Willbold, A. W. Hofmann, M. Amini, S. Aarburg, W. Abouchami, E. Hellebrand, B. Mocek, I. Raczek, A. Stracke, O. Alard, C. Bouman, S. Becker, M. Dücking, H. Brätz, R. Klemd, D. de Bruin, D. Canil, D. Cornell, C.-J. de Hoog, C. Dalpé, L. Danyushevsky, A. Eisenhauer, Y. Gao, J. E. Snow, N. Groschopf, D. Günther, C. Latkoczy, M. Guillong, E. H. Hauri, H. E. Höfer, Y. Lahaye, K. Horz, D. E. Jacob, S. A. Kasemann, A. J. R. Kent, T. Ludwig, T. Zack, P. R. D. Mason, A. Meixner, M. Rosner, K. Misawa, B. P. Nash, J. Pfänder, W. R. Premo, W. D. Sun, M. Tiepolo, R. Vannucci, T. Vennemann, D. Wayne and J. D. Woodhead, *Geochem., Geophys., Geosyst.*, 2006, **7**, 1–44.
18 S. Goderis, B. Soens, M. S. Huber, S. J. McKibbin, M. van Ginneken, F. Van Maldeghem, V. Debaille, R. C. Greenwood, I. A. Franchi, V. Cnudde, S. Van Malderen, F. Vanhaecke, C. Koeberl, D. Topa and P. Claeys, *Geochim. Cosmochim. Acta*, 2020, **270**, 112–143.
19 L. Hendriks and D. M. Mitrano, *Environ. Sci. Technol.*, 2023, **57**, 7263–7272.
20 T. Pettke, F. Oberli, A. Audétat, M. Guillong, A. C. Simon, J. J. Hanley and L. M. Klemm, *Ore Geol. Rev.*, 2012, **44**, 10–38.
21 M. Burger, L. Hendriks, J. Kaeslin, A. Gundlach-Graham, B. Hattendorf and D. Günther, *J. Anal. At. Spectrom.*, 2019, **34**, 135–146.
22 G. C. Eiden, C. J. Barinaga and D. W. Koppenaal, *Rapid Commun. Mass Spectrom.*, 1997, **11**, 37–42.
23 M. van Ginneken, M. J. Genge, L. Folco and R. P. Harvey, *Geochim. Cosmochim. Acta*, 2016, **179**, 1–31.
24 N. Dauphas and A. Pourmand, *Geochim. Cosmochim. Acta*, 2015, **163**, 234–261.